ICAS 2021 SHANGHAI
International Council of the Aeronautical Sciences
32nd Congress of the International Council of the Aeronautical Sciences
September 6-10, 2021
Pudong Shangri-La, Shanghai, China

ANALYSIS OF THRUST-SCALED ACOUSTIC EMISSIONS OF AIRCRAFT PROPELLERS AND THEIR DEPENDENCE ON PROPULSIVE EFFICIENCY

Xin Geng[1], Tianxiang Hu[1,2], Peiqing Liu[1], Tomas Sinnige[2] & Georg Eitelberg[2]

[1]Key Laboratory of Aero-Acoustics Ministry of Industry and Information Technology (Lu Shijia Laboratory), Beihang University (BUAA), Beijing, 100191, China.
[2]Flight Performance and Propulsion Section (FPP), Faculty of Aerospace Engineering, Delft University of Technology, 2629 HS Delft, The Netherlands.

Abstract

The increasing demand for short-range passenger air transport and the strong push for aircraft with electric propulsion has renewed research interest in propellers. Despite the unmatched aerodynamic efficiency of propellers, their relatively high noise emissions limit widespread application on aircraft. Previous research has not systematically addressed the tradeoff between aerodynamic and aeroacoustic performance. This paper presents the results of an optimization study aimed at minimizing propeller noise without compromising aerodynamic efficiency. In the optimization, a blade-element-momentum-theory (BEMT) model is utilized which accounts for the effects of blade sweep on the blade loading. This BEMT model is coupled to a frequency-domain code for tonal noise prediction. A novel scaling approach is presented to directly relate the propeller noise emissions to the propeller thrust. Dedicated wind-tunnel experiments were performed to validate the analysis models. Good agreement between numerical and experimental results is obtained at low to moderate blade loading conditions. The optimization study shows that the blade sweep is an important design parameter to simultaneously maximize aerodynamic and acoustic performance. Compared to a modern baseline design, a noise reduction of 2.9 dB is achieved without reduction in propeller efficiency.

Keywords: aircraft propulsion, propellers, aeroacoustics, multi-objective optimization, noise reduction

1. Introduction

Propeller performance is a topic long studied in the aviation industry, and it is well known that propellers can provide aircraft propulsion with exceptionally high propulsive efficiency. The increasing demand for short-range passenger transportation and aircraft with (distributed) electric propulsion has led to renewed interest in propellers by the research community. However, a major challenge needs to be overcome in order to enable widespread use of propellers: noise emissions. Contrary to turbofan engines, that feature engine casings with extensive acoustic liners, unducted propellers provide no means for noise attenuation. Instead, the noise generation needs to be mitigated at the source, by improving the blade design and operation.

In recent times, several studies have focused on broadband noise reductions for small-scale propellers, using techniques such as forced transition [1] and trailing-edge modifications such as serrations [2][3], which have been shown to indeed enable broadband noise reductions. Serrations are also widely investigated in the wind-turbine industry [4]. For high-speed propellers relevant to passenger aircraft, however, the major noise sources are of tonal nature, caused by the periodic passages of the loaded propeller blades [5]. Therefore, in order to achieve effective propeller noise reductions, the acoustic blade optimization should focus on the tonal noise component.

Multi-objective optimizations for minimum sound-pressure level and maximum aerodynamic efficiency have been performed by Marinus [6] using RANS simulations coupled with a time-domain acoustic solver. Others [7]- [9] have taken a similar approach with lower-fidelity aerodynamic analysis tools coupled to comparable acoustic solvers. The existing optimization studies indicate the potential improvements that can be achieved by optimizing the propeller design and operation. However, due to the black box nature of the optimization approaches involved, the results from these optimization

studies do not provide insight into the sensitivities of the blade performance to the design parameters. As such, they cannot provide effective design guidelines for propellers. To this end, sensitivity studies have been performed as well [10] [11], often investigating a subset of design variables with a one-variable-at-a-time approach. Most of the previous studies [6,7,10] show that the blade sweep angle is an important design parameter to reduce the noise emissions without significantly penalizing the aerodynamic efficiency of the propeller. The physical mechanism behind this noise reduction due to sweep is acoustic interference due to phase offsets between the acoustic waves emanating from the different blade sections [5]. In all previous work on propeller noise emissions, the acoustic data have been expressed in terms of the nondimensional sound pressure level and usually dimensional frequency. However, these are not scaling parameters, and therefore are unsuitable to compare propeller performance between different designs and scale from model scale to full scale in case of experimental activities.

The goal of this paper is to obtain acoustic scaling parameters to be able to describe the propeller noise emissions in terms of scaled amplitude and frequency, and subsequently use the newly defined scaling approach in an aerodynamic-acoustic optimization approach based on validated analysis tools. Fast, low-order aerodynamic and acoustic analysis methods were used in order to minimize turn-around time of the optimization routine, thereby making it suitable for preliminary design activities. Dedicated validation experiments were performed to benchmark the analysis tools. The optimization study focused on the blade sweep angle considering its potential in reducing the propeller noise emissions without penalizing aerodynamic performance.

The outline of the paper is as follows. The acoustic scaling is discussed in Section 2. Section 3 then describes the aerodynamic and acoustic analysis models. Subsequently, Section 4 describes the validation experiments, followed by the validation of the numerical models in Section 5. Section 6 then discusses the optimization study, after which conclusions are provided in Section 7.

2. Scaling of Propeller Noise Emissions

Most of the propeller noise emission measurement results are characteristically presented in terms of sound pressure level *SPL* vs. frequency *f*. An example is provided in Figure 1. The *SPL* is defined as a logarithmic variable, where the rms value of the measured pressure oscillation p_{rms} is normalized with a reference pressure for a given observed frequency range:

$$SPL = 20\log_{10}\frac{p_{rms}}{p_{ref}} \tag{1}$$

The frequency is often presented in an unscaled manner, in dimensions of Hz.

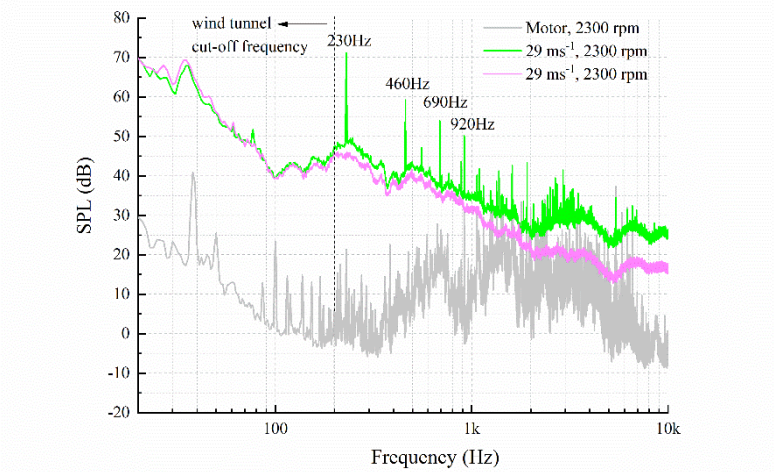

Figure 1 – Measured sound pressure level spectra of propeller noise in the far-field for various configurations.

Usually both the frequency range (20 Hz – 20 kHz) as well as the reference pressure p_{ref} = 20 µPa used to normalize the measured acoustic pressure originate from human audibility characteristics. They represent the frequency range and minimal pressure audible to healthy adults.

Considering the need to use ground based experiments to predict flight performance, scaling parameters for extrapolation to flight need to be derived. Human audibility is not a parameter that can be used for scaling. Therefore, a physics-based scaling approach was defined for scaling of propeller noise measurements.

For a preliminary analysis, we limit ourselves to the tonal components of the rotating propellers and ignore the variations in the broadband noise; the latter usually being orders of magnitude below the amplitude of the tonal noise observed at blade passing frequency (BPF) and its harmonics, see also the same figure 1 above. So instead of using a broadband reduced frequency formulation, only the frequency determined by the rotation speed of the propeller is scaled according to the Strouhal scaling:

$$Str = \frac{nD}{u_\infty} \tag{2}$$

In this formulation n is the rotational speed of the propeller, D is the diameter of the propeller and u_∞ is the freestream/flight velocity. In the further discussion, we choose to normalize the acoustic frequency with the blade passing frequency BPF, which is a blade number multiple of the rotational speed n. The Strouhal number will then be identically reproduced in the scaled experiment, when the geometrically similar propeller is operated at the same advance ratio J as the full-scale propeller. So, by fulfilling the advance ratio similarity we simultaneously obtain the Strouhal number similarity for the blade passing frequency as well. This means that the frequency of interest, the BPF, is a scalable parameter in the experiments and we can focus our discussion on that scaled frequency in the following.

In order to obtain also scalability for the noise amplitude at the scaled frequencies, we focus on the prime task of the propeller: producing thrust. In the actuator disk approximation, the thrust is the result of the pressure jump across the disk. Thus we want to evaluate the effect of the pressure jump across the actuator disk – the disk loading – on the generation of noise per type of propeller geometry. Thus, instead of presenting the acoustic pressure variations as a fraction of the audible pressure threshold, we present it as a dimensionless fraction Π of the disk loading:

$$\Pi = 20\log\frac{p_{rms}D^2}{T} \tag{3}$$

where T is the thrust of the propeller and D the diameter, as noted above. The dimensionless fraction defined by Equation 3 is referred to as thrust-specific sound pressure level (TSSP) in the remainder of the paper.

It is obvious that scaling with the thrust alone, while necessary, is not sufficient for scaling the acoustic behavior of the propeller. To start with, the thickness noise is present even when the thrust $T = 0$ at finite advance ratios and even in the windmilling conditions. This indicates that the Mach number dependence of the noise at the respective advance ratios J has to be accounted for in the scaling of propeller noise. This is because of the possibility to vary the inflow velocity and still maintain the advance ratio. Both for the thrust-scaled noise as well as for the thickness noise – the dominant contributors to the tonal components of noise – the Mach number scaling is imperative.

In the presented optimization process, the Mach number dependency was not further explored; only one freestream condition was considered. The propeller operating conditions were thus defined in terms of performance, the thrust (coefficient) and efficiency, as these were considered as sufficient to determine the aerodynamic behavior. For the acoustic optimization this means that the Mach number dependency is at present treated as an independent parameter. The validity of this treatment still needs to be verified in the future.

The difficulty to verify the above approach with the help of the current experiments is that the experiments were performed at constant angular frequency n and the advance ratio was varied by changing the freestream velocity. The optimization, on the other hand was performed at constant freestream Ma, while the advance ratio J was varied by changing the angular frequency n. Both approaches result in a Mach number variation, albeit in different ways and directions.

In a simplified approach, the Mach number scaling can either be obtained from the same theory due to Hanson [12] as applied in the design process discussed in the present paper, or from the even

more generic discussion as formulated by Lighthill in Crocker et al. [13] In this approach, the lifting surface, like the propeller blade in our approximation, produces noise which scales with the 6th power of the Mach number, see Hutcheson et al. [14] This would account for both the dipole as well as quadrupole contribution in the description of the noise generation mechanism. The experimental data will be analyzed in light of the above considerations.

3. Numerical analysis models

3.1 BEMT prediction of propeller performance

The propeller performance was predicted with a standard blade element momentum theory (BEMT) model [15], extended to account for the effects of blade sweep. The blade was divided into a set of 25 blade elements, and each blade element is treated as a two dimensional airfoil with its local flow schematics as presented in Figure 2.

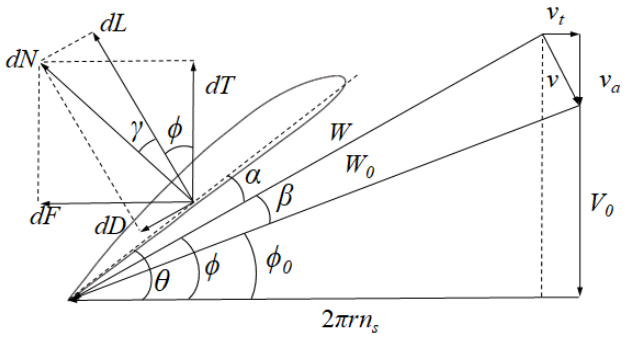

Figure 2 – Blade section with velocity triangle and resulting loading.

In Figure 2, V_0 is the incoming flow velocity, W is total kinematic velocity of the actual airflow, v_a is axial induced velocity, v_t is tangential induced velocity, n_s is the rotational speed in Hz, θ is pitch angle, β is the interference angle, α is the angle of attack, γ is the drag-to-lift angle, ϕ_0 is the airflow angle $\phi_0 = \tan^{-1}(V_0/2\pi r n_s)$. Based on this blade element model, the local thrust and torque can be written as:

$$\begin{cases} dT = \frac{1}{2}\rho V_0^2 \frac{c_l b(1+a)^2}{\sin^2\phi\cos\gamma}\cos(\phi+\gamma)dr \\ dQ = \frac{1}{2}\rho V_0^2 \frac{c_l b(1+a)^2}{\sin^2\phi\cos\gamma} r\sin(\phi+\gamma)dr \end{cases} \tag{4}$$

where a is the axial induction factor that is defined as $a = v_a/V_0$. According to the actuator disk theory, the local thrust and torque are also given by:

$$\begin{cases} dT = 4\pi r dr \rho {V_0}^2 (1+a)a \\ dQ = 4\pi\rho V_0 (1+a)(2\pi r n_s) a' r^2 dr \end{cases} \tag{5}$$

where a' is the tangential induction factor defined as $a' = v_t/2\pi r n_s$. Combining Eq.4 and 5 and re-arranging, the expression can be written as:

$$c_l\sigma = \frac{4\sin\phi\tan(\phi-\phi_0)}{1-\tan\gamma\tan(\phi-\phi_0)} \tag{6}$$

where c_l is the lift coefficient of blade element, $c_l = 2dL/(\rho W^2 b dr)$, and σ is the local blade solidity defined as $\sigma = N_B b/(2\pi r)$. In the present study, the aerodynamic performance of each blade element (lift and drag polars) were analyzed using XFOIL Version 6.99 in a viscous mode, in which both local Reynolds number and Mach number were considered with a transition setting at 0.1c downstream the leading-edge over both sides of the airfoil.

Eq.6 can be further simplified by substituting $\phi = \phi_0 - \beta$:

$$c_l\sigma = \frac{4\sin(\phi_0+\beta)\tan\beta}{1-\tan\gamma\tan\beta} \tag{7}$$

Eq.7 is an implicit equation, and can be solved for the interference angle β with a Newton-Raphson method. Once the interference angle is known, the induction factors in both the axial and tangential directions can be found from Eq.8:

$$\begin{cases} a = \frac{\tan\phi[1+\tan\phi_0\tan(\phi+\gamma)]}{\tan\phi_0[1+\tan\phi\tan(\phi+\gamma)]} - 1 \\ a' = \mathrm{atan}\phi_0\tan(\phi+\gamma) \end{cases} \tag{8}$$

Previous work by Burger [20] accounted for the impact of the sweep angle Λ on aerodynamic and acoustic propeller performance using the BEM implementation by Rosen and Gur [21] [22]. In this study, the sweep is defined by the mid chord line of the blade in the plane of rotation. The sweep is computed by drawing a line from each mid chord point on the airfoil stations towards the next. Then, a reference line parallel to the center line of the unswept blade is drawn which intersects the mid chord line. The angle between the parallel reference line and the mid chord line is the local angle of attack. Any out of plane translation for sweep or lean is not accounted for using this method. Consistent with [23], the midchord alignment (MCA) describes the deviation of the blade section midchord from the helicoid swept out by the pitch change axis. The geometric relationship between the Λ and MCA is:

$$\Lambda = \operatorname{atan}\frac{MCA}{r} \tag{10}$$

with r is the radial station of the blade section, as is depicted in Figure 3.

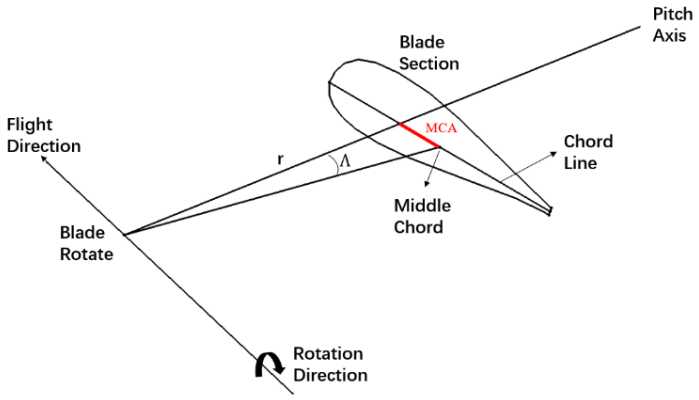

Figure 3 – Definition of midchord alignment (MCA).

Due to the addition of sweep, the spanwise extent of each blade section is adjusted. This is done by correcting *dr*, as can be seen in Equation (11):

$$dl = \frac{dr}{\cos\Lambda} \tag{11}$$

With *dl* known, the thrust and torque at each radial segment can be computed. The total thrust and torque are obtained by a simple summation of the values at each station:

$$\begin{cases} T = \frac{1}{2}\rho V_0^2 N_B \int_0^R \frac{c_l b(1+a)^2}{\sin^2\phi\cos\gamma}\cos(\phi+\gamma)dl \\ Q = \frac{1}{2}\rho V_0^2 N_B \int_0^R \frac{c_l b(1+a)^2}{\sin^2\phi\cos\gamma} r\sin(\phi+\gamma)dl \end{cases} \tag{12}$$

For the three-dimensional correction of the current BEMT model, a momentum loss factor *F* was implemented:

$$\mathcal{F} = \frac{2}{\pi}\cos^{-1}e^{-f} \tag{13}$$

where *f* is:

$$f = \frac{N_B}{2}\frac{R-r}{R\sin\phi} \tag{14}$$

3.2 Frequency-domain prediction of propeller noise

The current study only models the tonal component of the propeller noise. As will be shown later, this was an appropriate choice since the sound-pressure level of the measured tonal noise was about 20 dB above that of the broadband noise.

It is well-known that tonal propeller noise is composed of contributions from thickness and loading sources. The frequency-domain noise prediction method proposed by Hanson [12] was used to predict the far-field noise emissions from the propeller. In this analysis, the propeller noise waveform is Fourier transformed and expressed as:

$$p(t) = \sum_{m=-\infty}^{\infty} P_{mB}\exp[-imB\Omega_D t], \tag{15}$$

with P_{mB} the complex Fourier coefficient of the acoustic pressure, consisting of contributions due to blade volume (P_{Vm}), drag (P_{Dm}), and lift (P_{Lm}):

$$P_{mB} = P_{Vm} + P_{Dm} + \underline{P_{Lm}} \tag{16}$$

$$\begin{Bmatrix} P_{Vm} \\ P_{Dm} \\ P_{Lm} \end{Bmatrix} = -\frac{\rho_0 c_0^2 B \sin\theta \exp\left[imB\left(\frac{\Omega_D r}{c_0} - \frac{\pi}{2}\right)\right]}{8\pi \frac{y}{D}(1 - M_x \cos\theta)} \times$$

$$\int M_r^2 e^{i(\phi_0+\phi_s)} J_{mB}\left(\frac{mBzM_T \sin\theta}{1-M_x \cos\theta}\right) \begin{Bmatrix} k_x^2 t_b \Psi_V(k_x) \\ ik_x\ (c_d/2)\Psi_D(k_x) \\ -ik_y\ (c_l/2)\Psi_L(k_x) \end{Bmatrix} dz \tag{17}$$

4. Setup of validation experiments

4.1 Propeller model

As a reference for the analysis and optimization, a scaled propeller model was tested as shown in Figure 4. The propeller consists of six blades (N_B = 6), with an overall diameter of D = 0.6 m and a hub diameter of 0.2D. The distribution of the planform design parameters (relative chord length c/D, relative thickness t/c, twist angle χ and normalized sweep MCA/R) of the propeller along the radial direction are shown in Figure 5. The blades are characterized by nonzero and radially varying midchord alignment, and the thickness and twist angle of the blades gradually decrease along the radial direction. The chord length remains almost constant in the radial direction up to r/R = 0.65, and after that decreases rapidly toward the slender tip. The propeller was driven by a servo motor that can deliver 5 kW power at a maximum rotational speed of 3000 rpm.

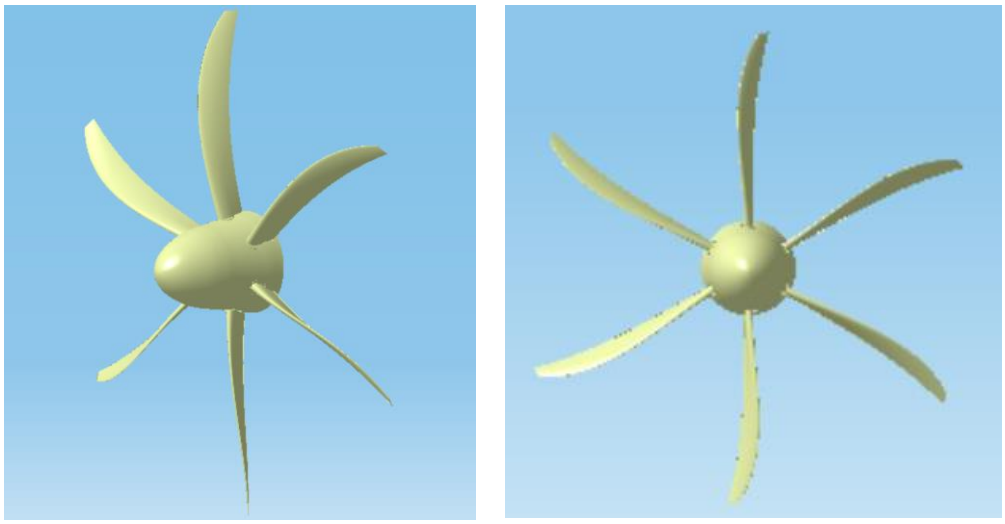

Figure 4 – CAD drawing of the test model propeller.

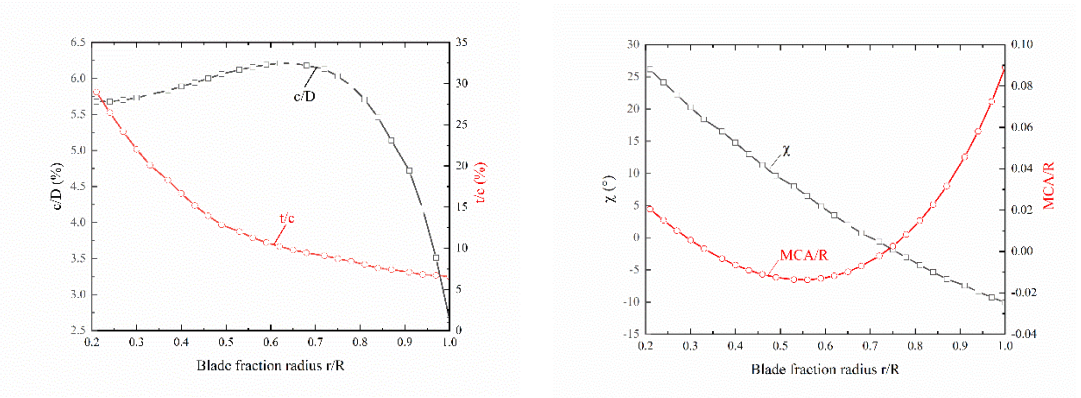

a) Chord (c/D) and thickness (t/c) b) twist (χ) and Sweep (MCA)

Figure 5 – Radial distributions of relative chord length c/D, relative thickness t/c, twist angle χ and normalized midchord alignment MCA/R of the propeller blade.

4.2 Wind-tunnel facility

The tests were conducted in Beihang's D5 acoustic wind tunnel. This closed-circuit, open-jet tunnel features a test section size of 1m (H) × 1m (W) × 2.5m (L) as shown in Figure 6. The test section is surrounded by an anechoic chamber to provide non-reflecting test conditions. The size of the anechoic chamber is 7 m (L) × 6 m (W) × 6 m (H), and the lower cut-off frequency is 200 Hz [16]. The background noise level at the frequencies of the BPF and its first four harmonics are 50.1, 43.6, 43.3, 37.4 and 32.6 dB, respectively (1BPF up to 5BPF). The experimental rig and inner surface of the open section collector were covered with sponge material to minimize acoustic interference.

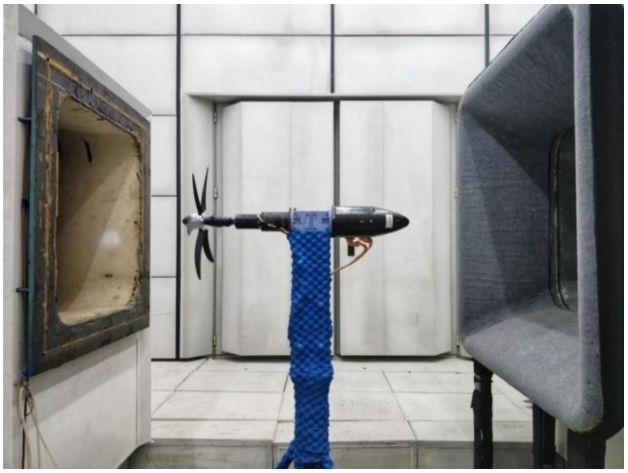

Figure 6 – Propeller performance test in D5 acoustic wind tunnel.

4.3 Measurement techniques

Measurements were taken of the integral forces produced by the propeller, as well as the acoustic emissions in the far field. The propeller performance (thrust, torque) was measured using a six-component beam strain-gauge balance mounted between the propeller and motor. The output signal from the force balance was fed into the data acquisition system via a slip-ring device. The data acquisition system consists of an analog-to-digital converter, a signal amplifier and a data acquiring computer. The test sample rate is 1 kHz, and the sample time 60 seconds for each test point.

The acoustic emissions from the propeller were measured with five far-field microphones, see Figure 7. Far-field noise was measured using a Brüel & Kjær 12-channel acoustic vibration analysis system, which includes a 12-channel compact LAN-XI module and 1/2 inch free-field microphones (type 4189). The free-field microphone sensitivity is 50 mV/Pa, and the input range is 14.6 - 146 dB. The acoustic signal was measured over a time interval of 41.75 seconds at a sampling frequency of 65,536 Hz. The far-field microphone array allowed the microphones to be placed 2.5 m (approx. 4 diameters) away from the geometric center of the propeller disk, with axial directivity angles between 50° and 145° (5° interval).

Figure 7 – The acoustic measurement setup for the test model propeller.

4.4 Operating conditions

The propeller performance measurements were taken at a freestream velocity range of V_∞ = 9 -35 ms^{-1} at constant RPM of 2300 (advance ratio range J = 0.4 – 1.8), over which the turbulence level was always below 0.08% of V_∞. The acoustic measurements were all performed at propeller angular speed of 2300 rpm and incoming flow speed V_∞ = 17, 21, 29 ms^{-1}, corresponding to (uncorrected) advance ratios of 0.74, 0.91, and 1.26, respectively. The pitch angle at r/R=0.7 was 36°.

The raw propeller performance data were reduced into non-dimensional scaling parameters advance ratio J, thrust coefficient C_T, power coefficient C_P, and propeller efficiency η:

$$J = V_c/(n_s D) \tag{18}$$

$$C_T = T/(\rho n_s^2 D^4) \tag{19}$$

$$C_P = 2\pi Q/(\rho n_s^2 D^5) \tag{20}$$

$$\eta = JC_T/C_P \tag{21}$$

where n_s = RPM/60 and V_c is the equivalent velocity which accounts for the change in inflow conditions in the wind tunnel due to the operation of the propeller. This effective velocity can be calculated by the following expressions [17]:

$$\frac{V_c}{V_\infty} = 1 - \frac{\tau k}{\sqrt{1+2\tau}} \tag{22}$$

$$\tau = \frac{T}{0.25\rho\pi D^2 V_\infty^2} \tag{23}$$

$$k = \frac{0.25\pi D^2}{S} \tag{24}$$

where V_∞ is the freestream velocity, τ is the equivalent thrust coefficient, k is the blockage ratio, and S is the area of the wind tunnel test section. All data presented are corrected by considering the corrected freestream velocity.

5. Validation results

5.1 BEMT prediction validation

The comparison between experimental and BEMT predicted results is shown in Figure 8. It can be seen that the BEMT method predicts the thrust coefficient of the test model propeller with a reasonable accuracy for J > 1.2. Since the rotational speed of the propeller was fixed, the variation in advance ratio was achieved by changing the incoming flow speed. Therefore, the conditions at low advance ratio correspond to low Reynolds numbers at the blade sections. For J < 1.2, the nonlinearity of the C_T curve becomes more obvious. Compared to the agreement for C_T, the BEMT predicted power coefficient and propulsive efficiency have more significant offsets even at high advance ratio. The maximum propulsive efficiency of the test model propeller was found at J = 1.35 in the experiment, while in the BEMT prediction it occurred at higher J due to the underestimation of the power coefficient. The power coefficient differed significantly at the higher advance ratios while the thrust was well captured. This suggests that the viscous effects were still underestimated in the BEMT analysis even in this region. At low advance ratios one would expect the BEMT to work less reliably than at high advance ratios, which in part is due to the dominance of radial forces at low J. Also the onset of three-dimensional stall is not captured. In the current study, the higher J cases have been chosen during the optimization. The radial forces that are relevant at low J can be neglected in these conditions. It is assumed that the aerodynamic prediction in these conditions is sufficiently accurate for appropriate prediction of the TSSP, considering the good agreement of the blade lift component which is a dominant source of the BPF noise during the prediction [12].

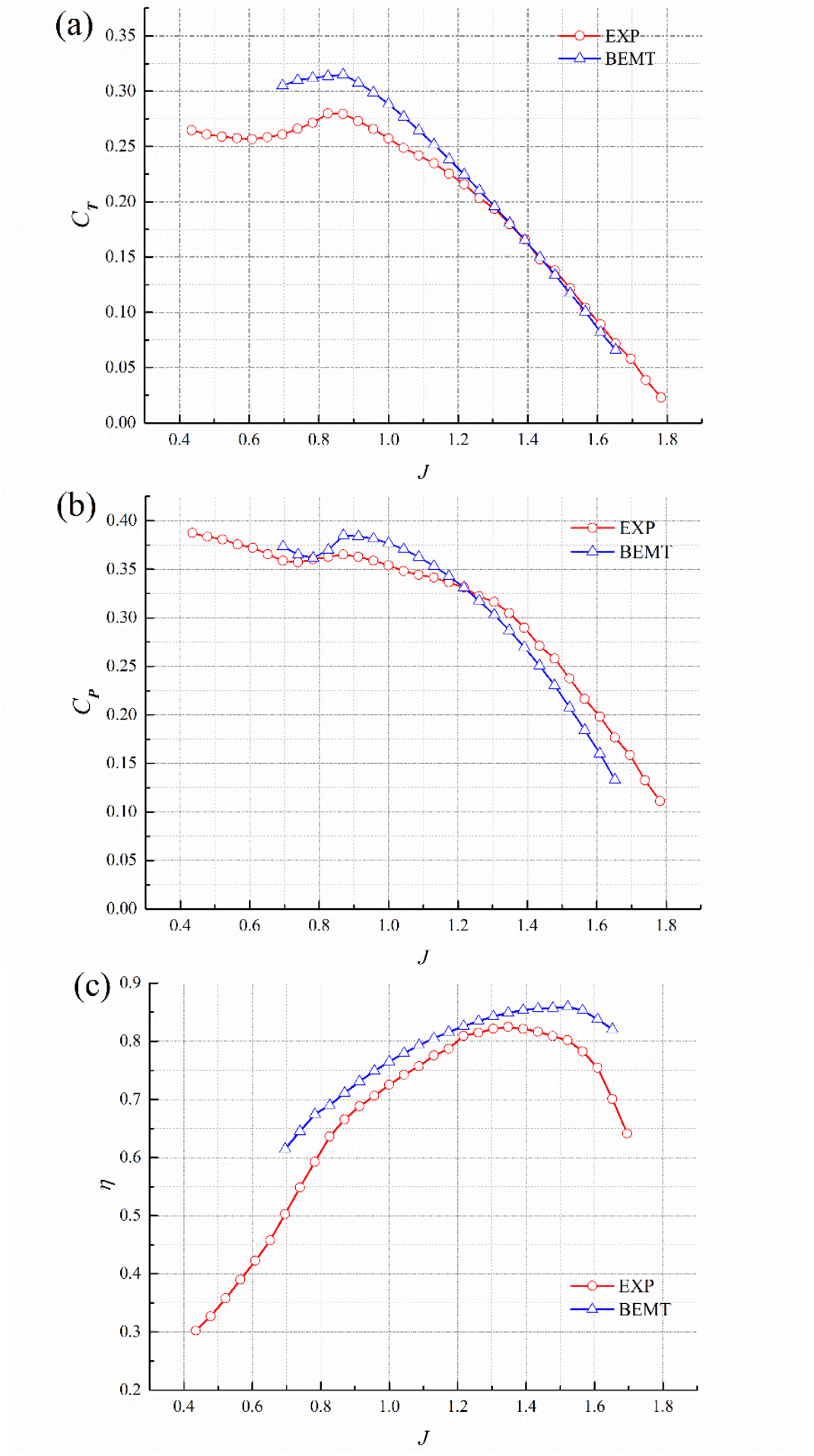

Figure 8 – Comparison between experimental (EXP) and BEMT predicted results of the test model propeller performance.

5.2 Validation of propeller noise prediction

The microphone signals were analyzed using a fast Fourier Transform. Figure 9 provides example spectra in terms of thrust specific sound pressure level (TSSP) versus frequency. Results are also provided for the motor-only (blades-off) and wind tunnel background noise. For comparison reasons, these were scaled with the thrust level measured for the blades-on case. The tonal component can be observed at the blade passing frequency (BPF=230 Hz) for all three incoming flow speed cases, and the corresponding TSSP at these three advance ratios are -68.91, -64.83 and -65.22 dB, respectively. When the advance ratio is 0.91 and 1.26, the TSSP value at the blade passing frequency is basically the same after the acoustic scaling, because the blade tip Mach number is not significantly different (0.2213 and 0.2290, respectively). As can be seen from the variation trend of the thrust coefficient with the advance ratio in the aerodynamic performance curves, when the advance ratio is 0.74, the blade is in the stall state, the surface flow is relatively complex and the thrust coefficient is in the nonlinear regime, so it cannot be applied directly to the acoustic scaling. Simultaneously, the amplitude of the broadband noise is the largest at this advance ratio, which is related to the turbulence noise caused by the complex flow field on the blade surface. Moreover, the higher harmonics of BPF are distinct at greater incoming flow speed.

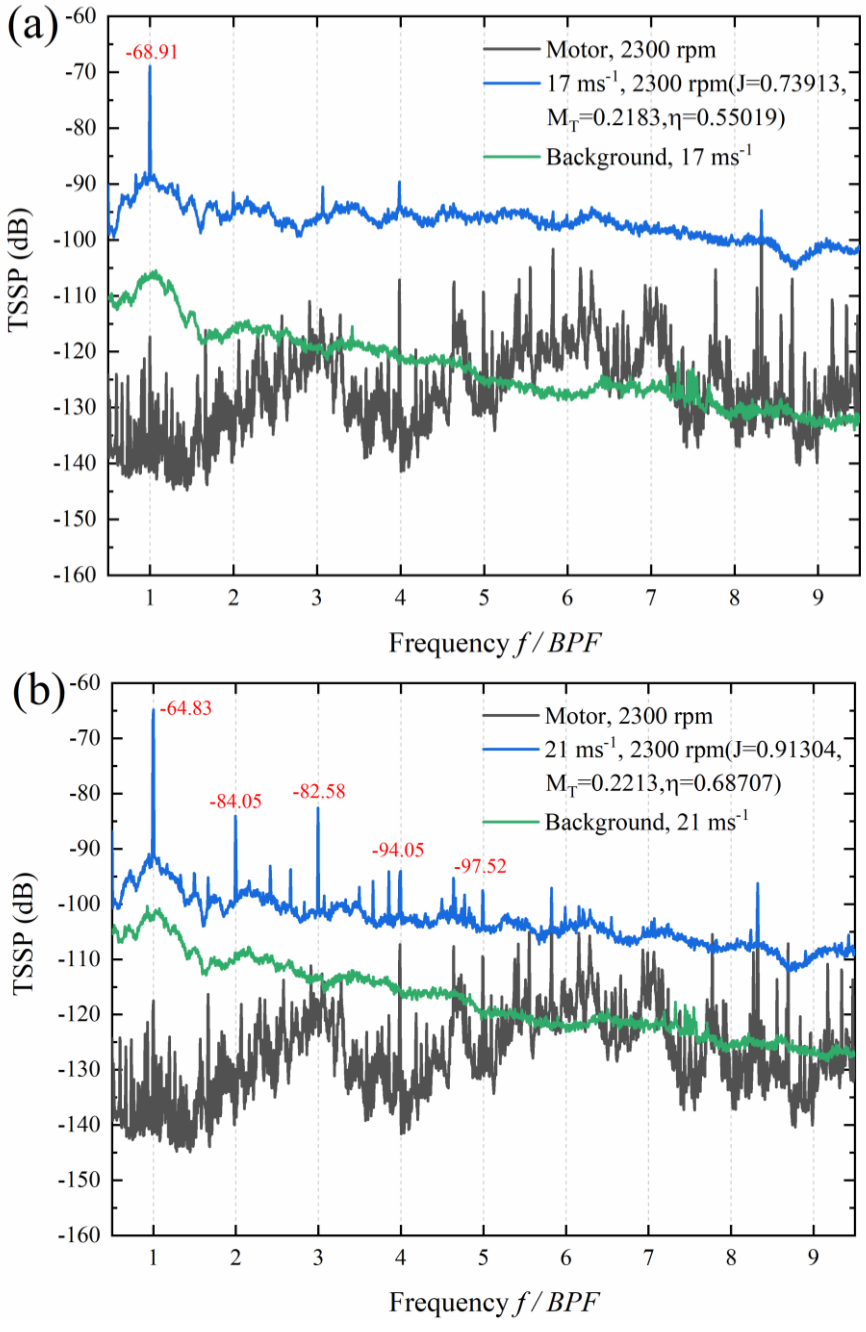

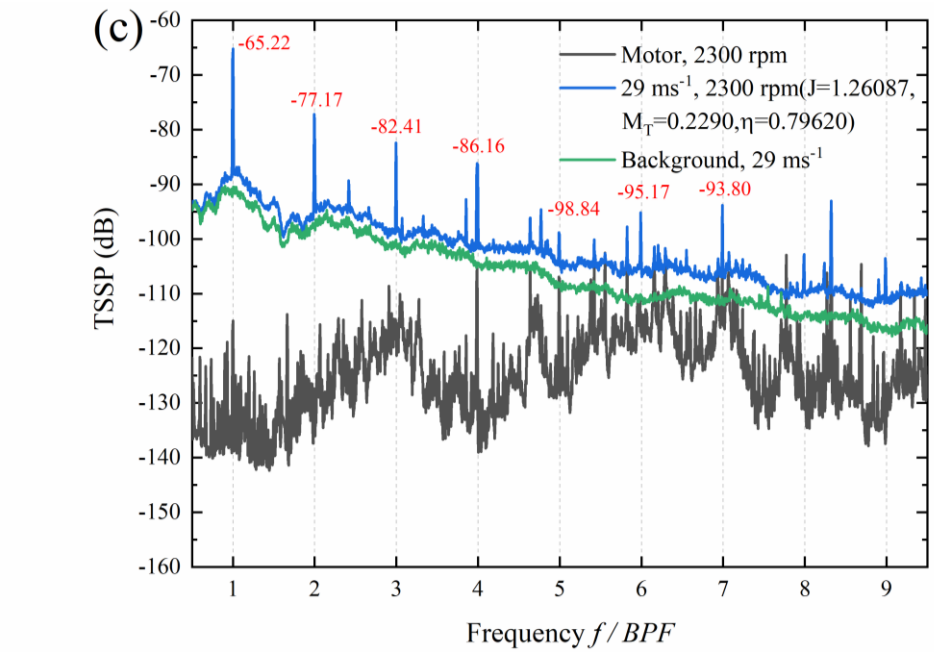

Figure 9 – TSSP of farfield noise with various incoming flow speeds at 90° directivity angle.

Figure 10 shows the directivity of the fundamental propeller tone (at 1BPF). When the directivity angle is between 50° and 130°, the TSSP value increases first and then decreases with increasing advance ratio. At an axial directivity angle of 100° at the farfield location, the TSSP value corresponding to the advance ratio of 1.09 is the largest (-63.74 dB), which is 2.65 dB larger than that corresponding to the advance ratio of 1.43.

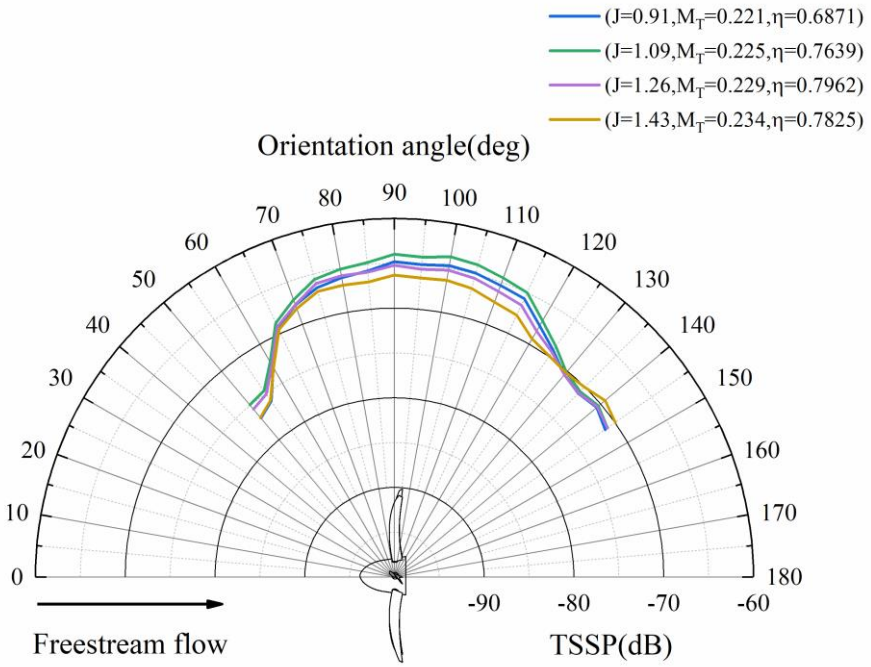

Figure 10 – The directivity (orientation angle = 50° - 145°) of TSSP (BPF = 1) at 2300 rpm and various incoming flow speeds.

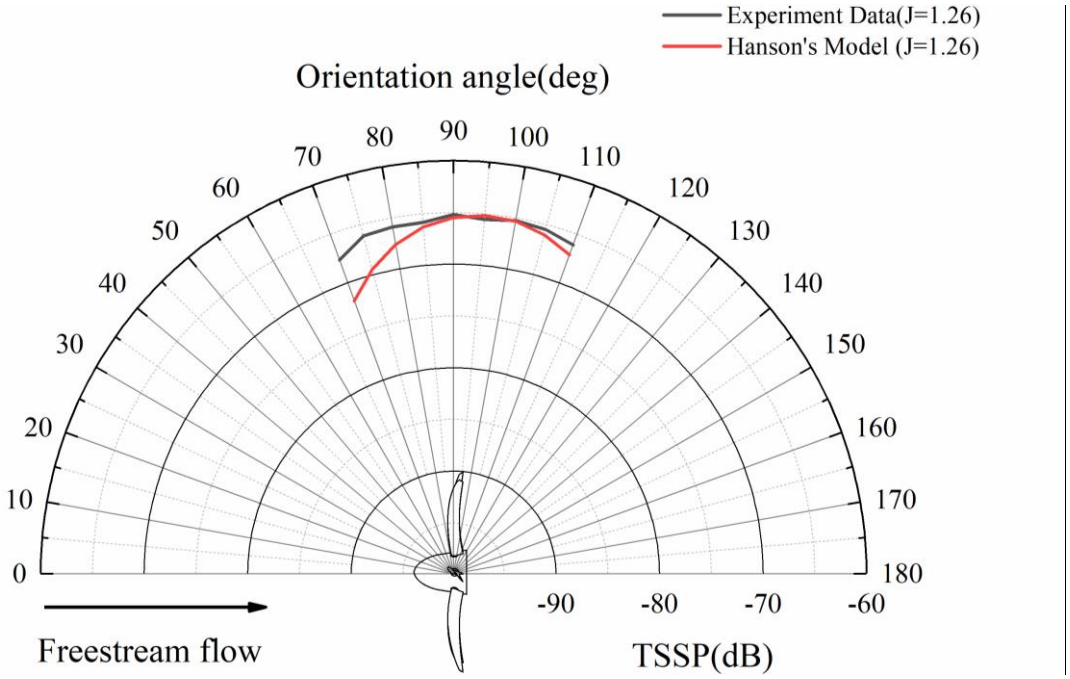

Figure 11 – The comparison between experimental and analytical results of the test model propeller noise at various orientation angles.

A comparison of the experimental data with the predicted results is provided in Figure 11. It can be seen that around the propeller plane, at an axial directivity angle near 90°, the analytical method provided a good accuracy with an offset of around 0.3dB. At the more upstream and downstream directivity positions, on the other hand, the offset between measured and predicted amplitude becomes more significant. It is expected that at low tip Mach number, as considered here, the frequency domain method is capable of capturing dipole noise sources (loading noise) of the overall noise emission, whereas other noise sources, for instance the thickness noise component were underestimated.

6. Optimization study

6.1 Optimizer architecture

Based on the above prediction methods, an integrated optimization design framework of propeller aerodynamic and aeroacoustic performance is established, as shown in Figure 12. The optimization was performed using an simulated annealing algorithm, which is based on the principle of solid annealing. At high temperatures, a large number of molecules in a solid move relatively freely between each other. If the solid cools slowly, the thermal motion of the particles decreases and gradually becomes ordered, reaching equilibrium at each temperature, and finally forming the crystal structure of the lowest energy state of the system. Simulated annealing is realized by using the Metropolis algorithm and controlling the temperature decline appropriately, and the searching direction is guided by the change of probability, so as to achieve the purpose of solving the global optimization problem. Accordingly, this concept is expressed computationally as follows [18]. First, the current state with design variable vector $\boldsymbol{x}^k$ and function value $f(\boldsymbol{x}^k)$ is chosen, after which a subsequent state with design variable vector $\boldsymbol{x}^p$ and function value $f(\boldsymbol{x}^p)$ is examined. The change in the function value between the current and probed states is denoted by $\Delta f(\boldsymbol{x}) = f(\boldsymbol{x}^p) - f(\boldsymbol{x}^k)$. The probed state is accepted with probability $P(\Delta f, T)$:

$$P(\Delta f, T) = \begin{cases} 1, & \text{if} \quad \Delta f(\boldsymbol{x}) \le 0 \\ \exp[-\Delta f(\boldsymbol{x})/T], & \text{otherwise} \end{cases} \tag{25}$$

where T denotes the temperature which is slowly reduced by the annealing process according to $T \rightarrow \alpha T$. Moreover, the parameter α represents the cooling rate and is set to 0.85 in this work. The

design variable vector in the probed state is obtained using a random walk procedure within a shrinking search boundary,

$$\boldsymbol{x}^{p} = \boldsymbol{x}^{k} + \left(\boldsymbol{x}_{\max} - \boldsymbol{x}^{k}\right) \times rand() \times T / T_0 - \left(\boldsymbol{x}^{k} - \boldsymbol{x}_{\min}\right) \times rand() \times T / T_0 \tag{26}$$

where $\boldsymbol{x}_{max}$ and $\boldsymbol{x}_{min}$ represent the maximum and minimum values of the design variable vector and T_0 denotes the initial temperature. The variable rand( ) is a random function that is uniformly distributed in the range [0, 1]. Equation (26) indicates that two random values are generated. The mathematical formulation used to update the design variable vector in the new state $\boldsymbol{x}^{k+1}$ is as follows:

$$\boldsymbol{x}^{k+1} = \boldsymbol{x}^{k} + u[-\Delta f(\boldsymbol{x})] \times \Delta \boldsymbol{x}^{k} + u[\Delta f(\boldsymbol{x})] \times u[P(\Delta f, T) - rand()] \times \Delta \boldsymbol{x}^{k} \tag{27}$$

where $\Delta \boldsymbol{x}^{k}$ denotes the change of vectors $\boldsymbol{x}^{p}$ and $\boldsymbol{x}^{k}$, such that $\Delta \boldsymbol{x}^{k} = \boldsymbol{x}^{p} - \boldsymbol{x}^{k}$. The value of the random function rand( ) is between zero and one. Moreover, the unit step function u[ ] is a discontinuous function that equals zero for negative inputs and otherwise is unity. In the current study, the Markov chain length is 100, the cooling down factor is 0.99, the perturbation factor is 0.01, the initial temperature is 300, the final temperature is 0.001 and the convergence residual is 1e-8.

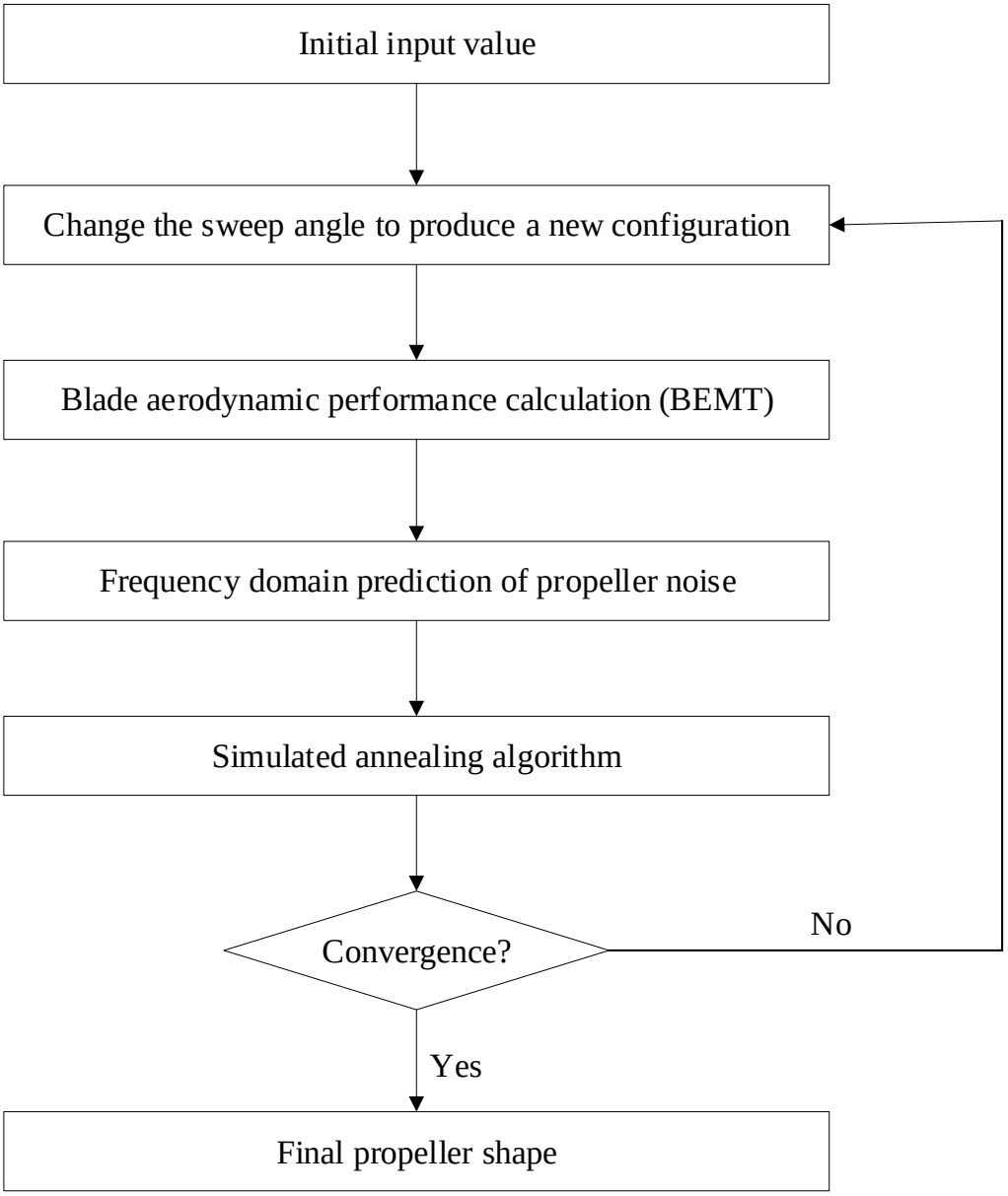

Figure 12 – Integrated optimization design framework of aerodynamics and aeroacoustics.

6.2 Operating Conditions, Objectives and Constraints

In the current study, a six-bladed propeller was optimized by using a classic simulated annealing algorithm with a consideration of both aerodynamic and aeroacoustic performances. As described above, the goal of the optimization study was to evaluate the potential of reducing the propeller noise while minimizing the cost of this reduction in terms of thrust performance and efficiency of propulsion. As a well-described baseline propeller the test model propeller could be used as a starting point (Section 4.1). The operation condition was set at a freestream velocity V_∞ = 29 ms^{-1} at constant RPM of 2300 (advance ratio J = 1.26).

The aerodynamic and aeroacoustic performances were predicted by BEMT and the frequency-domain prediction method respectively as aforementioned in Section 3. To achieve a quiet propeller design with minimum noise level, the thrust specific sound pressure level (TSSP) has been selected as the objective during the optimization. The value of the design variable sweep (MCA) at a given radial location r is determined through 4th order Bezier curve interpolation using the given five control points. The ordinates x_i of those control points, determining the shape of the variable midchord alignment distributions $x(r)$, are used as optimization parameters and are allowed to vary over specific intervals. In the optimization process the coordinates of the control points at both ends of the curve remain unchanged, and the coordinate value of the third control point is always smaller than that of the second and third control points. The blade twist and chord length distribution along the radial direction remain unchanged.

The final optimization design model is as follows [19]:

$$\min\left(\sum_{n}\mathbf{TSSP}_i / n\right)$$

$$\text{s.t.}\begin{cases} \eta_{\text{opt}} \geq \eta_{\text{org}} \\ C_{T\_\text{opt}} \geq C_{T\_\text{org}} \\ \left(TSSP_{\max}\right)_{\text{opt}} \leq \left(TSSP_{\max}\right)_{\text{org}} \\ TSSP_{\max} = \max\left(TSSP_1, \cdots TSSP_{\text{n}}\right) \end{cases} \tag{28}$$

with $TSSP_i$ (i=1,2,…,10) is obtained by energy superposition of the thrust specific sound pressure level in each frequency band. The index i indicates the considered monitoring point, distributed over the axial directivity range (25° up to and including 155°). A linear sum of TSSP values was used to not bias the optimization towards the region of maximum noise emissions (around the propeller plane). Future work should assess the impact of this choice on the overall noise hindrance during a typical flyover. $TSSP_{\max}$ is the maximum thrust specific sound pressure level at the monitoring point in the direction perpendicular to the axis of rotation and 2.5 meters from the center of the disk plane (θ = 90°), the subscript ‘‘org” represents the original propeller blade, and the subscript ‘‘opt” represents the propeller blade in the optimization design process.

6.3 Results

Figure 13 shows the geometric shape comparison between original (ORG) and the optimized (OPT) design. The radial distribution of dimensionless sweep (MCA/R) has been plotted in Figure 14. It can be seen that the maximum sweep location has been shifted from r/R = 0.55 to 0.49, at which the value of the MCA/R has been decreased by -0.01268 (from -0.01362 to -0.02648). Moreover, at r/R = 0.76, the dimensionless sweep of these two designs is similar. The individual OPT has a larger forward sweep than the individual ORG from root to 76% radius, and the former also has a little larger sweep from 76% radius to the tip.

Table 1 shows the propeller thrust coefficient C_T, efficiency η, thrust specific sound pressure level at θ = 90° $TSSP_{\pi/2}$ and average thrust specific sound pressure level $TSSP_{\text{overall}}$, $TSSP_{overall} = 10 \times \log_{10}\left[\int_{5/36\pi}^{31/36\pi}\left(\frac{p_{rms}\cdot D^2}{T}\right)^2 d\theta\right]$, of the original and optimized designs . Compared with

the ORG configuration, the OPT configuration has no reduction in efficiency and thrust coefficient, and a 6.22 dB reduction in average thrust specific sound pressure level.

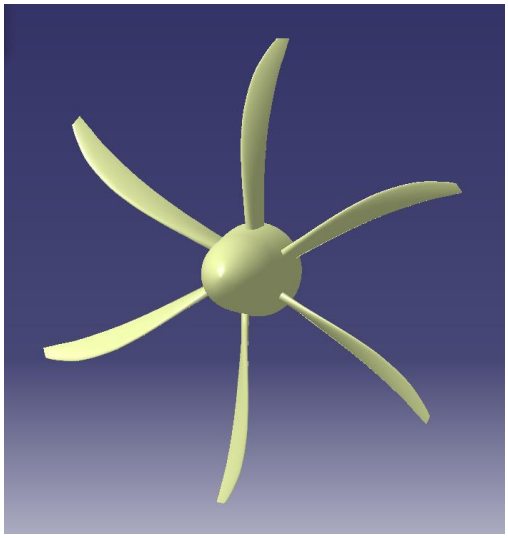

a) Original Propeller(ORG)

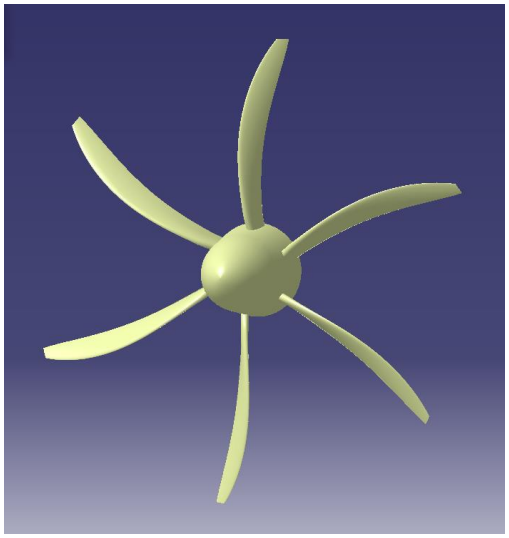

b) Optimized Propeller(OPT)

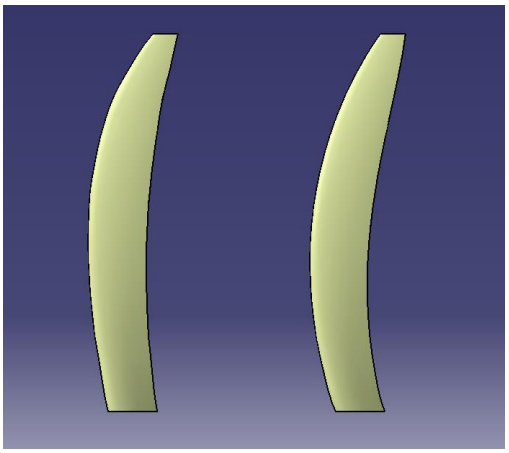

c) Comparison of the ORG and OPT blade planform shapes

Figure 13 – Comparison of original and optimized propeller geometries.

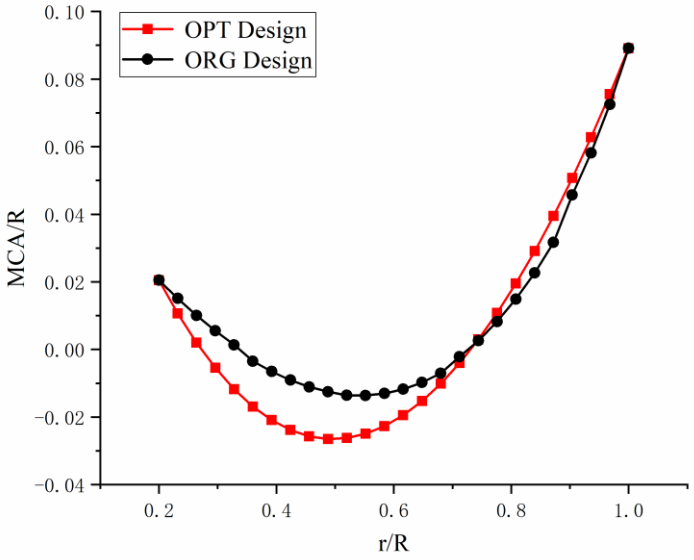

Figure 14 – Original and optimized radial distributions of blade sweep (midchord alignment).

Figure 15 presents a comparison of the thrust specific sound pressure level (TSSP) at each monitoring point between the OPT configuration and the ORG configuration. From the view of the whole axial directivity distribution, the thrust specific sound pressure level (TSSP) of the ORG configuration of the monitoring point at 95° is the largest and the value is -65.18 dB. For the OPT configuration a 2.9 dB noise reduction is obtained, while the corresponding directivity angle of the maximum TSSP shifts to 85°. The noise reduction is effective from θ = 50° up to 155°. As a deviation from the overall trend, the TSSP of the OPT configuration obtained in the upstream direction is slightly higher than that of the ORG configuration, albeit at very low sound pressures. This may be a side-effect of the change in the radial sweep distribution. The reduced average TSSP level, quantified by $TSSP_{overall}$, confirms that the OPT design is a low-noise configuration. As discussed by Hanson [12], the effect of sweep is to cause some phase cancellation between spanwise segments of the blade. This has been exploited by the optimization algorithm in the current study.

Table 1 – Comparison of original and optimized design results

	Original	**Optimized**
C_T	**0.2103**	**0.2215**
η	**0.8349**	**0.8453**
$TSSP_{\pi/2}$ **(dB)**	**-65.49**	**-68.49**
$TSSP_{overall}$ **(dB)**	**6.74**	**0.52**

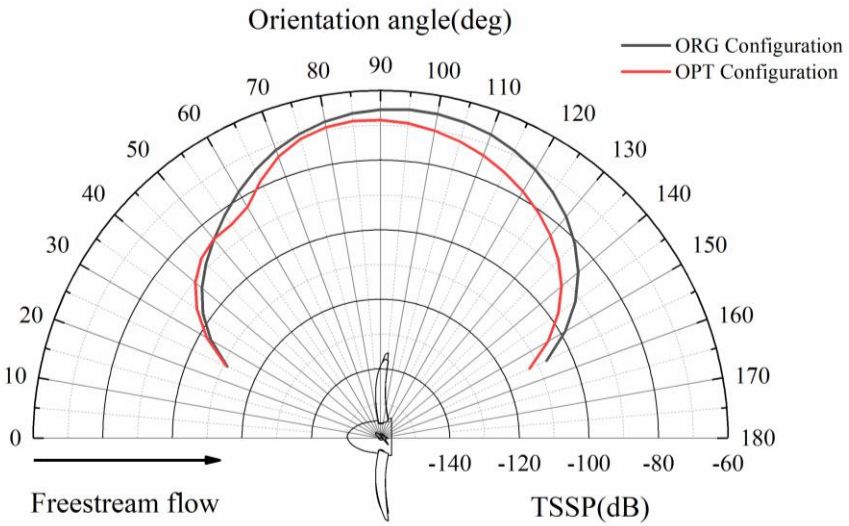

Figure 15 – Comparison of thrust specific sound pressure fluctuation (TSSP) before and after optimal design.

7. Conclusions

Instead of presenting the acoustic pressure variations as a fraction of the audible pressure threshold, a novel scaling approach has been proposed to directly relate the propeller noise emissions to the propeller thrust. Compared to the experimental aerodynamic performance, the BEMT method predicts the thrust coefficient of the propeller with a reasonable accuracy at low to moderate loading conditions (high advance ratio). In the current study, this high advance ratio case has been chosen during the optimization. It is assumed that the TSSP is well presented because of the agreement of the lift which is a dominant source of the BPF noise during the acoustic prediction. The noise results

show that around the propeller plane, at an axial directivity angle near 90°, the analytical method provided a good accuracy with an offset of around 0.3 dB from the experimental data. The original propeller design was optimized using a classic simulated annealing algorithm with a consideration of both aerodynamic and aeroacoustic performances. The value of the design variable sweep at a given radial location is determined through 4th order Bezier curve interpolation using the given five control points. An improved propeller design with no loss of aerodynamic performance and reduction of thrust specific sound pressure level was obtained through an optimization design process, and the maximum thrust specific sound pressure level at the monitoring point was reduced by 2.9 dB compared to the modern baseline design; the same reduction in noise level was obtained when integrating the TSSP over the semi-circle of all axial directivity angles considered. This points to an overall reduction in acoustic emissions achieved through the optimized blade sweep distribution.

References

[1] Leslie, A., Wong, K. C., Auld, D., “Broadband noise reduction on a mini-UAV Propeller”, 14th AIAA/CEAS Aeroacoustics Conference, AIAA Paper 2008-3069, 2008.

[2] Yang, Y., Li, Y., Liu, Y., Arcondoulis, E. J. G., Wang, Y., Huang, B., Li, W., “Aeroacoustic and aerodynamic investigation of multicopter rotors with serrated trailing edges”, 25th AIAA/CEAS Aeroacoustics Conference, AIAA Paper 2019-2523, 2019.

[3] Ning, Z., Wlezien, R., Hu, H., “An Experimental Study on Small UAV Propellers with Serrated Trailing Edges”, 47th AIAA Fluid Dynamics Conference, AIAA Paper 2017-3813, 2017.

[4] Oerlemans, S., Fisher, M., Maeder, T., Kögler, K., “Reduction of Wind Turbine Noise Using Optimized Airfoils and Trailing-Edge Serrations”, AIAA Journal, Vol. 47, No. 6, 2019, pp. 1470-1481.

[5] Magliozzi, B., Hanson, D. B., Amiet, R. K., “Propeller and Propfan Noise”. In: Hubbard, H. H. (ed.): Aeroacoustics of Flight Vehicles: Theory and Practice – Volume 1: Noise Sources, NASA Langley Research Center, 1991, pp. 1-64.

[6] Marinus, B., “Multidisciplinary Optimization of Aircraft Propeller Blades”, PhD thesis, École Centrale de Lyon, 2011.

[7] Pagano, A., Federico, L., Barbarino, M., Guida, F., Aversano, M., “Multi-Objective Aeroacoustic Optimization of an Aircraft Propeller”, 12th AIAA/ISSMO Multidisciplinary Analysis and Optimization Conference, AIAA Paper 2008-6059, 2008.

[8] Gur, O., Rosen, A., “Optimization of Propeller Based Propulsion System”, Journal of Aircraft, Vol. 46, No. 1, 2009, pp. 95-106.

[9] Ingraham, D., Gray, J., Lopes, L. V., “Gradient-Based Propeller Optimization with Acoustic Constraints”, AIAA Scitech 2019 Forum, AIAA Paper 2019-1219, 2019.

[10] Miller, C. J., Sullivan, J. P., “Noise constraints effecting optimal propeller designs”, SAE General Aviation Aircraft Meeting and Exposition, 1985.

[11] Yang, L., Huang, J., Yi, M., Zhang, C., Xiao, Q., “A numerical study on the effects of design parameters on the acoustics noise of a high efficiency propeller”, Acoustical Physics, Vol. 65, No. 6, 2017, pp. 699-710.

[12] Hanson, D. B., “Helicoidal Surface Theory for Harmonic Noise of Propellers in the Far Field”, AIAA Journal, Vol. 18, No. 10, 1980.

[13] Malcolm J. Crocker, Editor-in-Chief, Handbook of Acoustics, John Wiley and Sons, 1998 ISNB 0-471-25293-X

[14] Hutcheson, F. V., Brooks, T. F., Burley, C. L., Stead, D. J., “Measurement of the Noise Resulting from the Interaction of Turbulence with a Lifting Surface”, International Journal of Aeroacoustics, Vol. 11, No. 5-6, 2012, pp. 675-700.

[15] Liu, X., He, W., “Performance Calculation and Design of Stratospheric Propeller”, IEEE Access, Vol. 5, 2017, pp. 14358-14368.

[16] Liu, P., Xing, Y., Guo, H., Li, L., “Design and performance of a small-scale aeroacoustic wind tunnel”, Applied Acoustics, Vol. 116, 2017, pp. 65–69.

[17] Liu, Z., Liu, P., Hu, T., Qu, Q., “Experimental investigations on high altitude airship propellers with blade planform variations”, Proceedings of the Institution of Mechanical Engineers, Part G: Journal of Aerospace Engineering, Vol. 232, No. 16, 2018, pp. 2952-2960.

[18] Liu, J.-L., “Novel Taguchi-Simulated Annealing Method Applied to Airfoil and Wing Planform Optimization”, Journal of Aircraft, Vol. 43, No. 1, 2006.

[19] Yu. P., Peng, J., Bai, J., Han, X., Song, X., "Aeroacoustic and aerodynamic optimization of propeller blades", Chinese Journal of Aeronautics, Vol. 33, No. 3. 2020, pp. 826-839.

[20] Burger, S., “Multi-Fidelity Aerodynamic and Aeroacoustic Sensitivity Study of Isolated Propellers”, Master thesis, Delft University of Engineering, 2020.

[21] A. Rosen and O. Gur, “Novel approach to axisymmetric actuator disk modeling”, AIAA Journal, Vol. 46, No. 11, 2008, pp. 2914–2925.

[22] O. Gur and A. Rosen, “Comparison between blade-element models of propellers”, Aeronautical Journal, Vol. 112, No. 1138, 2008, pp. 689–704.

[23] Whitfield, C. E., Mani, R., Gliebe, P. R., "High speed turboprop aeroacoustic study (single rotation). Volume 1: Model development." (1989).

Copyright Statement